Supporting Information for

Encapsulation of a $[Dy(OH_2)_8]^{3+}$ cation: magneto-optical and theoretical studies of a caged, emissive SMM displaying slow relaxation

M. Al Hareri,[a] E.L. Gavey,[a] J. Regier,[a] Z. Ras Ali[a], L.D. Carlos,[b] R.A.S. Ferreira,[b] and M. Pilkington*[a]

[a] Department of Chemistry, Brock University
1812 Sir Isaac Brock Way
St Catharines, ON
Canada, L2S 3A1
Tel: +1 (905) 688 5550; Ext. 3403
E-mail: mpilkington@brocku.ca

[b] Department of Physics and CICECO Institute of Materials
University of Aveiro
3810-193, Aveiro, Portugal.

Table of Contents

S-1 Synthesis of $[Dy(H_2O)_8(Bz\text{-}15C5)_3](ClO_4)_3$ (4)

All reagents were purchased from Sigma-Aldrich and used without further purification. Infrared spectra were recorded on a Bruker Alpha FT-IR spectrometer. UV-vis data were obtained using a Beckman Coulter DU 720 General-Purpose UV-vis spectrophotometer. Mass spectrometry data were recorded on a Carlo Erba/Kratos EC/MS acquisition system and processed at a SPARC workstation. Elemental analysis measurements were performed by Atlantic Microlab Inc., Norcross, GA, USA.

Benzo-15-crown-5 (1 eq., 31.8 mg, 1.20 mmol) was added in one portion to a solution of $Dy(ClO_4)_{3(aq)}$ (40% w/w, 1 eq., 0.924 mL, 1.20 mmol) in MeOH/MeCN (1:3, 30 mL). The solution was heated to 55°C and vigorously stirred for 3 h. After cooling to r.t., the solution was filtered through cotton wool and left to crystallize by slow evaporation. After 2 weeks, complex **(4)** was isolated as clear orange single crystals suitable for X-ray diffraction (37.0 mg, 22.1%). IR (cm^{-1}): 3520 (br), 3241 (b), 2926 (w), 2870 (w), 1659 (w), 1595 (m), 1250 (m), 1124 (s), 934 (s), 758 (s). UV-vis (MeOH, nm)**:** λ_{max} **= 224** (ε = 4700 L mol^{-1} cm^{-1})**.** MS(ESI): *m/z* 1275.87 $[(Dy(OH_2)_8](benzo\text{-}15C5)_3ClO_4.EtOH{\cdot}H_2O]^+$. Anal. cald for $C_{42}H_{74}O_{35}Cl_3Dy$: C, 35.83; H, 5.30; N, 0.00; Found C, 36.00; H, 5.27; N, 0.00%.

Fig. 1 ESI Mass spectrometry data for (4) (1:1 Dithranol matrix 10mg/mL)

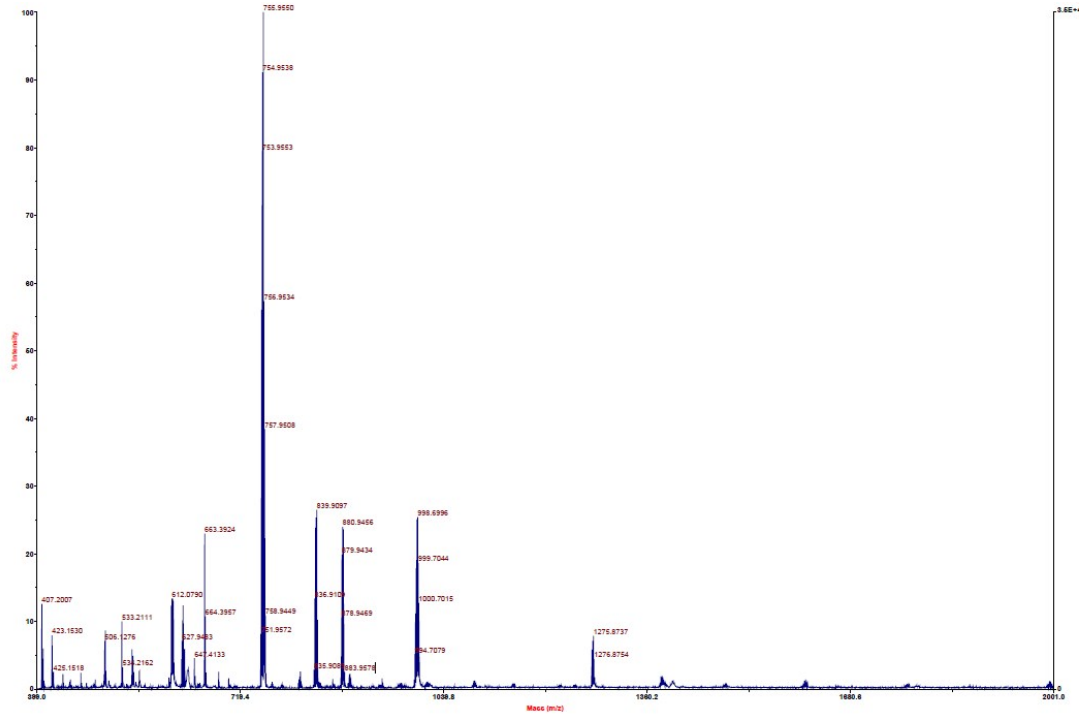

S-2 Crystallographic data and SHAPE analysis for (4)

2.1 X-ray crystallography data

Single crystals of (**4**) were mounted in a cryoloop with paratone oil and examined on a Bruker APEX-II CCD diffractometer equipped with a CCD area detector and an Oxford Cryoflex low temperature device. Data were measured at 150(2) K with Mo-Kα radiation (λ = 0.71073 Å) using the APEX-II software.[1] Cell refinement and data-reduction were carried out by SAINT. An absorption correction was performed by the multi-scan method implemented in SADABS.[2] The structure of (**4**) was solved by direct methods SHELXS-97 and refined using SHELXL-2014 in the Bruker SHELXTL suite.[3] Hydrogen atoms were added at calculated positions and refined with a riding model.

Table 2.1 Crystallographic data for (4)

Chemical formula	$3(C_{14}H_{20}O_5)\cdot DyH_{16}O_8\cdot 3(ClO_4)$
M_r	1409.87
Crystal system, space group	Triclinic, $P^{-}1$
Temperature (K)	150
a, *b*, *c* (Å)	12.741 (3), 13.235 (4), 17.923 (4)
α, β, γ (°)	89.94 (1), 85.741 (10), 86.594 (11)
V (Å^3)	3008.7 (13)
Z	2
Radiation type	Mo *K*α
μ (mm^{-1})	1.47
Crystal size (mm)	0.29 × 0.27 × 0.23
Data collection	
Diffractometer	Bruker Apex II CCD detector diffractometer
Absorption correction	Multi-scan Bruker *SADABS*
T_{min}, T_{max}	0.571, 0.747
No. of measured, independent and observed [$I > 2\sigma(I)$] reflections	80643, 14436, 13382
R_{int}	0.043
$(\sin\theta/\lambda)_{max}$ (Å^{-1})	0.668
Refinement	
$R[F^2 > 2\sigma(F^2)]$, $wR(F^2)$, S	0.069, 0.179, 1.09
No. of reflections	14436

No. of parameters	694
No. of restraints	22
H-atom treatment	H atoms treated by a mixture of independent and constrained refinement $w = 1/[\sigma^2(F_o^2) + (0.0838P)^2 + 28.6356P]$ where $P = (F_o^2 + 2F_c^2)/3$
$\Delta\rho_{max}$, $\Delta\rho_{min}$ (e Å^{-3})	4.51, −2.58

Table 2.2 Selected geometric parameters for (4)

Bond	Length (Å)	Bond	Lemgth (Å)
Dy1—O1	2.321 (4)	O19—C34	1.376 (11)
Dy1—O7	2.333 (4)	O19—C35	1.384 (13)
Dy1—O3	2.362 (5)	O20—C36	1.257 (13)
Dy1—O5	2.364 (4)	O20—C37	1.490 (14)
Dy1—O4	2.378 (4)	O21—C39	1.426 (12)
Dy1—O8	2.388 (5)	O21—C38	1.498 (13)
Dy1—O2	2.392 (4)	O22—C41	1.425 (10)
Dy1—O6	2.404 (4)	O22—C40	1.434 (10)
Cl1—O25	1.434 (5)	O23—C29	1.358 (9)
Cl1—O27	1.438 (5)	O23—C42	1.421 (11)
Cl1—O26	1.439 (5)	C1—C2	1.407 (11)
Cl1—O24	1.457 (5)	C1—C6	1.411 (13)
Cl2—O31	1.421 (5)	C2—C3	1.386 (14)
Cl2—O28	1.423 (6)	C3—C4	1.365 (19)
Cl2—O30	1.446 (5)	C4—C5	1.399 (17)
Cl2—O29	1.446 (6)	C5—C6	1.403 (11)
Cl3—O35	1.357 (8)	C7—C8	1.492 (13)
Cl3—O34	1.422 (7)	C9—C10	1.499 (12)
Cl3—O33	1.427 (8)	C11—C12	1.499 (10)
Cl3—O32	1.517 (9)	C13—C14	1.508 (13)
O9—C6	1.379 (11)	C15—C16	1.374 (9)
O9—C7	1.475 (10)	C15—C20	1.394 (9)
O10—C9	1.433 (11)	C16—C17	1.404 (11)
O10—C8	1.445 (10)	C17—C18	1.376 (12)
O11—C10	1.424 (10)	C18—C19	1.394 (11)
O11—C11	1.424 (9)	C19—C20	1.391 (9)
O12—C13	1.415 (9)	C21—C22	1.484 (10)
O12—C12	1.439 (8)	C23—C24	1.509 (10)
O13—C1	1.373 (9)	C25—C26	1.516 (11)

O13—C14	1.430 (11)	C27—C28	1.494 (10)
O14—C20	1.379 (8)	C29—C30	1.389 (10)
O14—C21	1.428 (8)	C29—C34	1.402 (10)
O15—C23	1.424 (8)	C30—C31	1.396 (12)
O15—C22	1.435 (7)	C31—C32	1.368 (13)
O16—C24	1.417 (8)	C32—C33	1.394 (12)
O16—C25	1.444 (8)	C33—C34	1.364 (13)
O17—C26	1.427 (8)	C35—C36	1.487 (14)
O17—C27	1.431 (8)	C37—C38	1.461 (18)
O18—C15	1.368 (8)	C39—C40	1.513 (14)
O18—C28	1.414 (8)	C41—C42	1.497 (12)

Bond	**Angle** (°)	**Bond**	**Angle** (°)
O1—Dy1—O7	81.65 (16)	C39—O21—C38	119.5 (8)
O1—Dy1—O3	103.17 (17)	C41—O22—C40	113.0 (6)
O7—Dy1—O3	144.70 (16)	C29—O23—C42	119.5 (6)
O1—Dy1—O5	146.80 (16)	O13—C1—C2	123.0 (8)
O7—Dy1—O5	109.43 (17)	O13—C1—C6	115.9 (7)
O3—Dy1—O5	85.79 (17)	C2—C1—C6	121.0 (8)
O1—Dy1—O4	77.13 (16)	C3—C2—C1	118.7 (10)
O7—Dy1—O4	142.95 (16)	C4—C3—C2	121.2 (10)
O3—Dy1—O4	70.59 (16)	C3—C4—C5	121.0 (9)
O5—Dy1—O4	75.95 (15)	C4—C5—C6	119.8 (11)
O1—Dy1—O8	80.55 (16)	O9—C6—C5	124.8 (9)
O7—Dy1—O8	72.01 (16)	O9—C6—C1	116.7 (7)
O3—Dy1—O8	143.18 (16)	C5—C6—C1	118.4 (9)
O5—Dy1—O8	73.92 (17)	O9—C7—C8	106.4 (7)
O4—Dy1—O8	74.79 (16)	O10—C8—C7	109.7 (7)
O1—Dy1—O2	74.73 (15)	O10—C9—C10	109.6 (7)
O7—Dy1—O2	74.35 (16)	O11—C10—C9	107.5 (7)
O3—Dy1—O2	73.39 (15)	O11—C11—C12	106.4 (6)
O5—Dy1—O2	137.92 (16)	O12—C12—C11	108.1 (5)
O4—Dy1—O2	126.99 (15)	O12—C13—C14	113.4 (6)
O8—Dy1—O2	140.57 (16)	O13—C14—C13	107.0 (7)
O1—Dy1—O6	142.81 (16)	O18—C15—C16	125.5 (6)
O7—Dy1—O6	75.81 (17)	O18—C15—C20	114.2 (5)
O3—Dy1—O6	80.43 (19)	C16—C15—C20	120.3 (6)
O5—Dy1—O6	69.77 (17)	C15—C16—C17	119.0 (7)
O4—Dy1—O6	136.26 (16)	C18—C17—C16	121.1 (7)

O8—Dy1—O6	118.71 (18)	C17—C18—C19	119.8 (7)
O2—Dy1—O6	70.94 (16)	C20—C19—C18	119.3 (7)
O25—Cl1—O27	109.7 (3)	O14—C20—C19	124.5 (6)
O25—Cl1—O26	109.4 (4)	O14—C20—C15	114.9 (6)
O27—Cl1—O26	110.5 (3)	C19—C20—C15	120.5 (6)
O25—Cl1—O24	108.4 (4)	O14—C21—C22	107.3 (5)
O27—Cl1—O24	109.2 (3)	O15—C22—C21	109.6 (5)
O26—Cl1—O24	109.8 (3)	O15—C23—C24	114.1 (5)
O31—Cl2—O28	110.4 (4)	O16—C24—C23	109.3 (5)
O31—Cl2—O30	110.5 (3)	O16—C25—C26	108.3 (5)
O28—Cl2—O30	109.0 (4)	O17—C26—C25	113.3 (5)
O31—Cl2—O29	110.9 (4)	O17—C27—C28	109.5 (5)
O28—Cl2—O29	108.8 (5)	O18—C28—C27	106.3 (6)
O30—Cl2—O29	107.2 (3)	O23—C29—C30	125.9 (7)
O35—Cl3—O34	112.5 (4)	O23—C29—C34	115.5 (6)
O35—Cl3—O33	117.2 (5)	C30—C29—C34	118.6 (7)
O34—Cl3—O33	110.4 (4)	C29—C30—C31	119.3 (7)
O35—Cl3—O32	106.6 (5)	C32—C31—C30	121.4 (8)
O34—Cl3—O32	105.9 (5)	C31—C32—C33	119.3 (8)
O33—Cl3—O32	103.1 (5)	C34—C33—C32	120.0 (8)
C6—O9—C7	128.7 (7)	C33—C34—O19	123.2 (8)
C9—O10—C8	115.0 (6)	C33—C34—C29	121.3 (7)
C10—O11—C11	112.6 (6)	O19—C34—C29	115.4 (8)
C13—O12—C12	113.9 (6)	O19—C35—C36	114.3 (10)
C1—O13—C14	119.0 (7)	O20—C36—C35	114.6 (10)
C20—O14—C21	118.7 (5)	C38—C37—O20	118.1 (10)
C23—O15—C22	114.5 (5)	C37—C38—O21	111.2 (9)
C24—O16—C25	112.1 (5)	O21—C39—C40	110.0 (7)
C26—O17—C27	113.9 (5)	O22—C40—C39	113.8 (8)
C15—O18—C28	120.1 (5)	O22—C41—C42	108.1 (6)
C34—O19—C35	119.4 (8)	O23—C42—C41	107.0 (8)
C36—O20—C37	114.5 (10)		

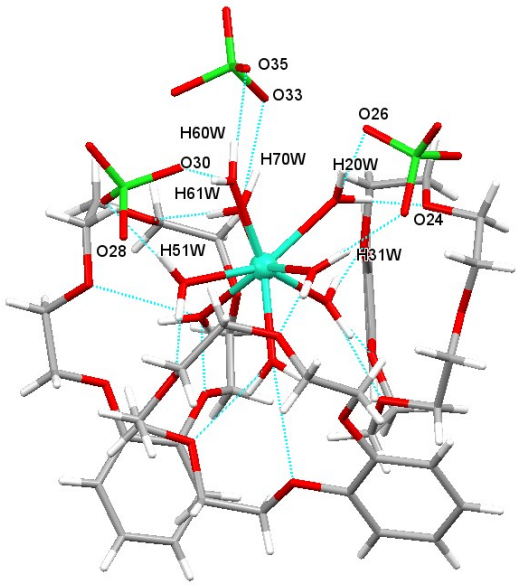

Fig. 2.1 Molecular structure of $[Dy(OH_2)_8](benzo\text{-}15C5)_3\cdot(ClO_4)_3$ (4) showing the H-bonding interactions to the perchlorate anions.

Table 2.3 H-bonding interactions for (4)

D-A	D-H...A (Å)	D···A (Å)	D-H···A (°)
O(1)-H(10W)···O(9)	1.99(3)	2.942(7)	172(8)
O(1)-H(10W) ···O(13)	2.58(8)	2.951(8)	103(6)
O(1)-H(11W) ···O(12)	1.76(6)	2.709(5)	169(9)
O(1)-H(11W) ···O(13)	2.51(8)	2.951(8)	108(6)
O(2)-H(20W) ···O(26)	1.96(7)	2.913(7)	166(7)
O(2)-H(21W) ···O(10)	1.73(7)	2.696(7)	177(8)
O(3)-H(30W) ···O(15)	1.73(4)	2.684(8)	173(8)
O(3)-H(31W) ···O(24)	1.82(6)	2.779(8)	170(6)
O(4)-H(40W) ···O(14)	2.14(9)	3.073(6)	165(7)
O(4)-H(40W) ···O(18)	2.54(9)	3.012(6)	107(5)
O(4)-H(41W) ···O(17)	1.85(8)	2.766(6)	156(8)
O(4)-H(41W) ···O(18)	2.58(8)	3.012(6)	107(5)
O(5)-H(50W) ···O(16)	1.73(6)	2.693(6)	172(4)
O(5)-H(51W) ···O(29)	1.98(6)	2.917(8)	169((9)
O(6)-H(60W) ···O(35)	1.92(6)	2.887(8)	172(4)

O(6)-H(61W) ···O(30)	1.85(5)	2.806(8)	171(8)
O(7)-H(70W) ···O(33)	1.83(7)	2.765(8)	163(8)
O(7)-H(71W) ···O(21)	1.71(8)	2.670(9)	172(9)
O(8)-H(80W) ···O(19)	2.04(8)	2.889(10)	148(7)
O(8)-H(80W) ···O(20)	2.56(7)	3.353(9)	140(6)
O(8)-H(81W) ···O(22)	1.97(7)	2.807(7)	144(8)
O(8)-H(81W) ···O(23)	2.31(7)	3.083(8)	136(8)

2.2 SHAPE parameters[4]

Continuous shape measures (CSMs) of the 8-coordinate Dy^{III} coordination polyhedron in complex (**4**). The value in red indicates the closest polyhedron according to the CSMs.

Polyhedron	Symmetry	Dy^{III} CSM
OP-8	D_{8h}	29.80
HPY-8	C_{7v}	23.54
HBPY-8	D_{6h}	16.31
CU-8	O_h	10.87
SAPR-8	D_{4d}	0.84
TDD-8	D_{2d}	1.28
JGBF-8	D_{2d}	14.40
JETBPY-8	D_{3h}	28.13
JBTPR-8	C_{2v}	1.88
BTPR-8	C_{2v}	1.34
JSD-8	D_{2d}	3.44
TT-8	T_d	11.56
ETBPY-8	D_{3h}	24.26

Abbreviations: OP-8, Octagon; HPY-8, Heptagonal pyramid; HBPY-8, Hexagonal pyramid; CU-8, Cube; SAPR-8, Square antiprism; TDD-8, Triangular dodecahedron; JGBF-8, Johnson gyrobifastigium; JETBPY-8, Johnson elongated triangular bipyramid J14; JBTPR-8, Biaugmented trigonal prism J50; BTPR-8, Biaugmented trigonal prism; TT-8, Triakis tetrahedron; ETBPY-8, Elongated trigonal bipyramid.

Fig. 2.2 Coordination geometry of the $[Dy(OH_2)_8]^{3+}$ cation superimposed on an idealized square antiprism.

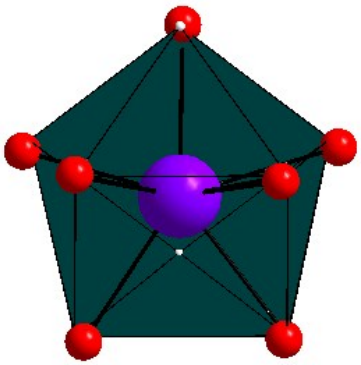

S-3 Magnetic data for (4)

Note: unless otherwise stated, solid lines are a guide for the eyes only.

Dc measurements were performed using a Quantum Design SQUID MPMS magnetometer in an applied field of 0.1 T, from 2 – 300 K. Ac measurements were carried out on a Quantum Design PPMS, in an oscillating field of 3.5 Oe, from 2 – 15 K. A range of frequencies between 50 and 10,000 Hz were used, in applied dc fields ranging from 0 to 1500 Oe. Measurements were performed on polycrystalline samples of **(4)**.

3.1 DC data

Fig. 3.1a Plot of χT *vs.* temperature for **(4)** from 2 - 300 K, with an average value of χT above 100 K of 13.90 $cm^3 \cdot K \cdot mol^{-1}$.

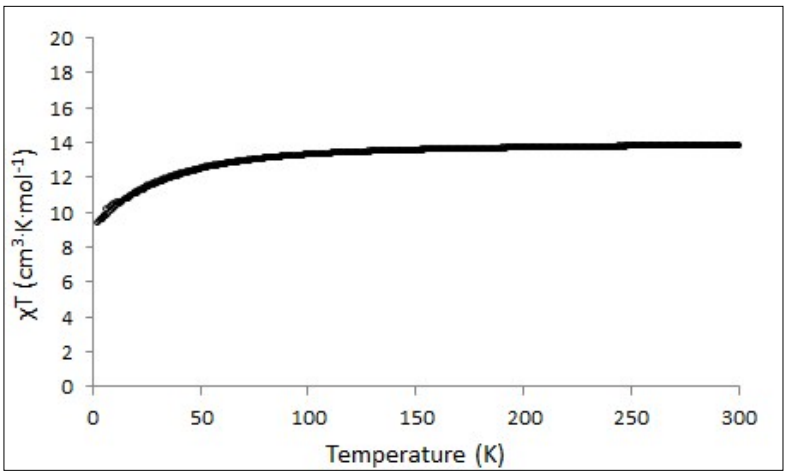

Fig. 3.1b Plot of 1/χ vs. temperature for **(4)** from 2 - 300 K. The black line is a best-fit to the Curie-Weiss law, giving *C* = 14.14 $cm^3 \cdot K \cdot mol^{-1}$ and a Weiss constant of 5.43 K.

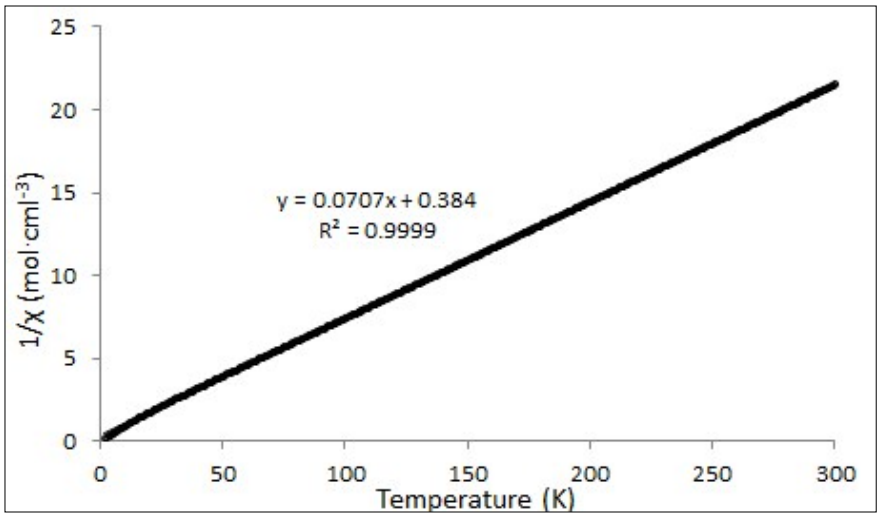

3.2 Additional ac data

Fig. 3.2a Plot of χ''_M *vs* temperature for **(4)** in zero dc field below 8 K, showing frequency dependent susceptibility but a lack of resolved maxima.

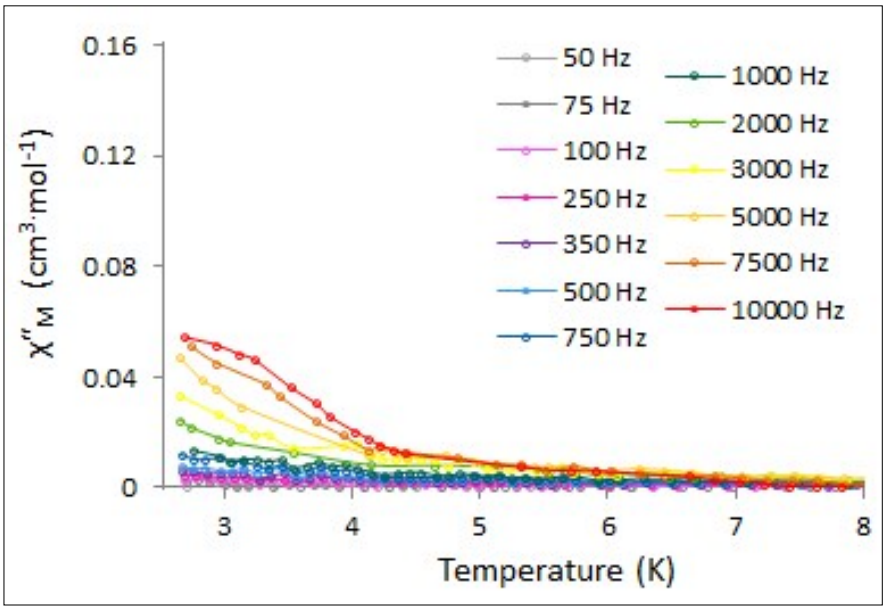

Fig. 3.2b Plot of χ''_M *vs* temperature for **(4)** in applied dc fields of 300, 800 and 1500 Oe, below 15 K.

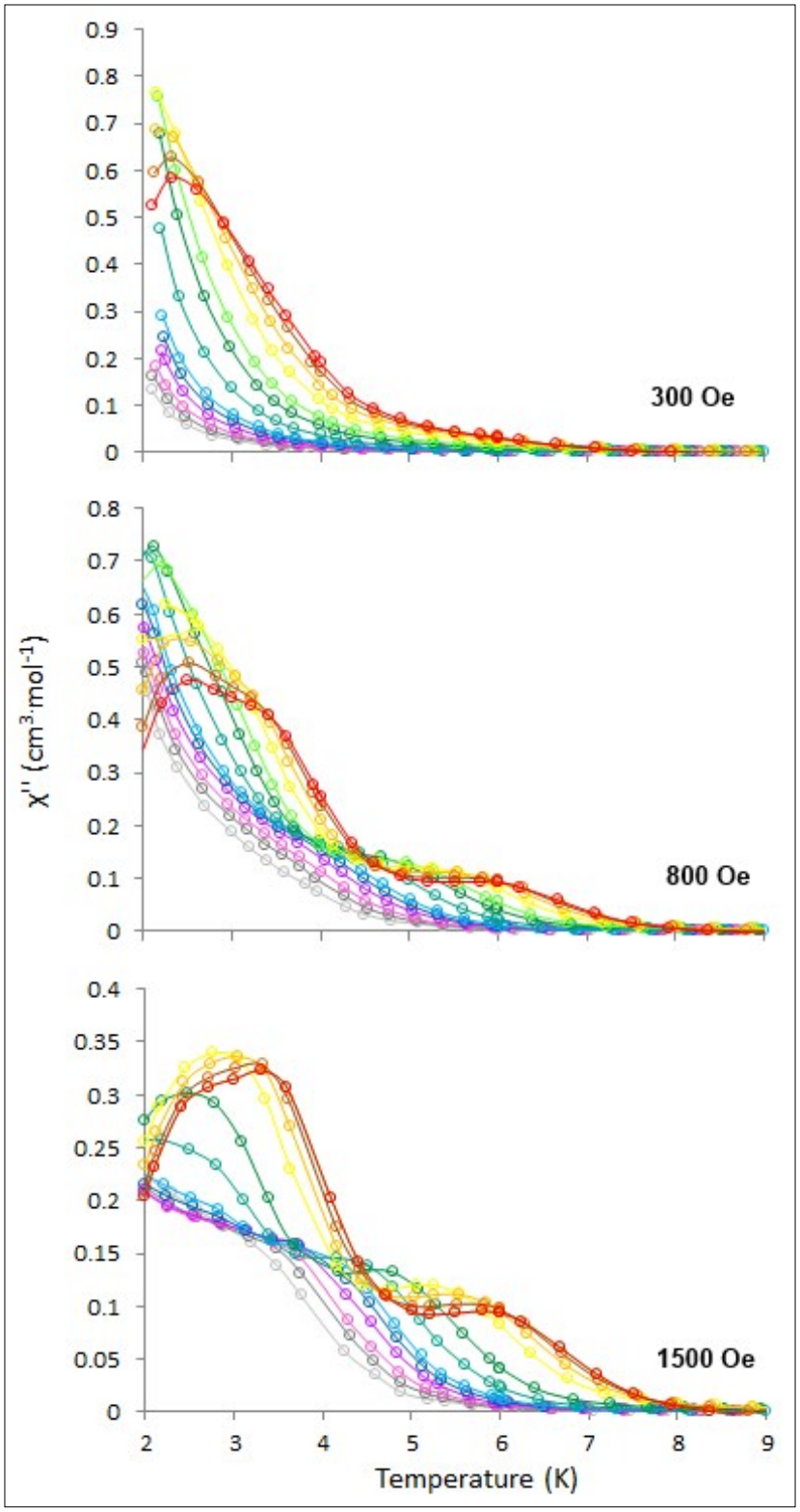

3.3 Fit to the Arrhenius law

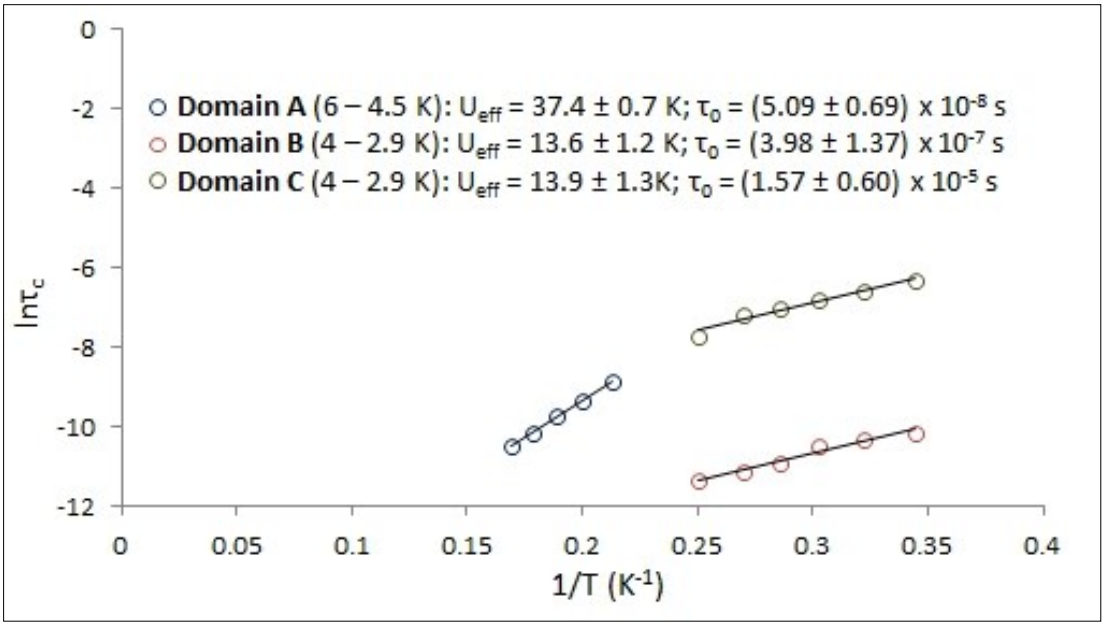

Fig. 3.3 Temperature dependence of the relaxation time for (**4**) at "high" (6.0 - 4.5 K) temperature, blue circles – domain A and "low" (4.0 – 2.9 K) temperatures, red and green circles – domains B and C respectively, under a static field of 800 Oe. The solid lines represent a fit to the Arrhenius law.

Please note that in the case of the Arrhenius plot we have included only the temperature regimes which could be modelled using a one or two component Cole-Cole/Debye equation. We appreciate that affords large gaps between 0.2 to 0.25 K^{-1} points, but the data in this region could not be modelled, since this is a transition region in which the susceptibility data collected over various frequencies at each temperature point has contributions from both the low temperature domains and the single high temperature domain. Hence, neither the one- nor the two-component equation accurately describes the observed data in this region.

S-4 Equations[5]

The Cole-Cole model describes the ac susceptibility as:

$$\chi(\omega) = \chi_S + \frac{\chi_T - \chi_S}{1 + (i\omega\tau_c)^{1-\alpha}} \qquad \textbf{Eqn. 1}$$

where $\omega = 2\pi f$, χ_T is the isothermal susceptibility, χ_S is the adiabatic susceptibility, τ_c is the temperature-dependent relaxation time, and α is a measure of the dispersivity of

relaxation times, with α = 0 reflecting a single Debye-like relaxation time and α = 1 reflecting an infinitely wide dispersion of τ_c values.

Dividing Eqn. 1 into its in-phase and out-of-phase components gives:

$$\chi'(\omega) = \chi_S + \frac{(\chi_T - \chi_S)}{2}\left\{1 - \frac{sinh[(1-\alpha)ln(\omega\tau_c)]}{cosh[(1-\alpha)\ln(\omega\tau_c)] + cos\left[{}^{1}/_{2}(1-\alpha)\pi\right]}\right\} \quad \textbf{Eqn. 2}$$

$$\chi''(\omega) = \frac{(\chi_T - \chi_S)}{2}\left\{1 - \frac{sin\left[{}^{1}/_{2}(1-\alpha)\pi\right]}{cosh[(1-\alpha)\ln(\omega\tau_c)] + cos\left[{}^{1}/_{2}(1-\alpha)\pi\right]}\right\} \quad \textbf{Eqn. 3}$$

In the case of complex **(4)**, the susceptibility behavior below 5 K is due to contributions from two distinct relaxation pathways. The relaxation in this temperature region can thus be described by the sum of two combined, modified Debye functions:

$$\chi(\omega) = \chi_{S1} + \frac{\chi_{T1} - \chi_{S1}}{1 + (i\omega\tau_{c1})^{1-\alpha 1}} + \chi_{S2} + \frac{\chi_{T2} - \chi_{S1}}{1 + (i\omega\tau_{c2})^{1-\alpha 2}} \quad \textbf{Eqn. 4}$$

Dividing Eqn. 4 into its in-phase and out-of-phase components gives:

$$\chi'(\omega) = \chi_S + (\chi_{T1} - \chi_S)\left\{\frac{1 + (\omega\tau_{c1})^{1-\alpha_1}\sin(\pi\alpha_1/2)}{1 + (\omega\tau_{c1})^{1-\alpha_1}\sin(\pi\alpha_1/2) + (\omega\tau_{c1})^{2-2\alpha_1}}\right\} \quad \textbf{Eqn. 5}$$

$$+ (\chi_{T2} - \chi_S)\left\{\frac{1 + (\omega\tau_{c2})^{1-\alpha_2}\sin(\pi\alpha_2/2)}{1 + (\omega\tau_{c2})^{1-\alpha_2}\sin(\pi\alpha_2/2) + (\omega\tau_{c2})^{2-2\alpha_2}}\right\}$$

$$\chi''(\omega) = (\chi_{T1} - \chi_S)\left\{\frac{1 + (\omega\tau_{c1})^{1-\alpha_1}\cos(\pi\alpha_1/2)}{1 + (\omega\tau_{c1})^{1-\alpha_1}\sin(\pi\alpha_1/2) + (\omega\tau_{c1})^{2-2\alpha_1}}\right\} \quad \textbf{Eqn. 6}$$

$$+ (\chi_{T2} - \chi_S)\left\{\frac{1 + (\omega\tau_{c2})^{1-\alpha_2}\cos(\pi\alpha_2/2)}{1 + (\omega\tau_{c2})^{1-\alpha_2}\sin(\pi\alpha_2/2) + (\omega\tau_{c2})^{2-2\alpha_2}}\right\}$$

where $\chi_S = \chi_{S1} + \chi_{S2}$

The Arrhenius equation, relating relaxation time τ_c to temperature T, is given by:

$$\tau_c = \tau_0 e^{U_{eff}/k_B T}$$ **Eqn. 7**

where τ_o is the tunneling rate and U_{eff} is the effective energy barrier.

S-5 Quantum chemical calculations

5.1 Experimental

The calculations were performed using the coordinates determined from single crystal X-ray diffraction without any further geometry optimizations. Two structural models were considered, the first was the full model with three hydrogen bonded benzo-15crown5 macrocycles and three perchlorate counter-anions (**Model 1**), the second model considered only the effects of the coordinating ligands (**Model 2**). *Ab initio* calculations of the CASSCF + RASSI/SINGLE_ANISO type were performed to evaluate the electronic structure of the Dy^{III} ion in the complex using the MOLCAS 8 quantum chemistry package.[6] The complete active space approach was used where the active space was chosen to include the 9 electrons of the 7 *4f* orbitals. Relativistic basis sets from the ANO-RCC library were used exclusively for all calculations where two types of basis sets (long and short) were used for each model as listed in tables 1a and b. Relativistic contractions are also taken into account through the use of the Douglas-Kroll-Hess Hamiltonian. Strong, spin-orbit coupling was included in the CASSI procedure which uses the spin-free Eigenstates of the CASSCF procedure as the elements in the state interaction determinant. In the CASSCF procedure, 21 roots were used for the sextets and 224 roots were used for the quartets. The doublet configurations were omitted due to limited computer resources. In the state interaction procedure, all 21 roots of the sextets were used and only 80 of the 224 quartet roots were used for Model 1 long due to hardware restrictions and 128 quartet roots were used for all other models. A comparison between the results generated with sextets only and the mixing of sextets and quartets for model 1 long, showed that the high energy quartet configurations do not affect the magnitude of the energy levels and the properties of the low energy excited states to any significant degree. The g-tensors of each of the Kramers doublets were calculated using the S=1/2 pseudo-spin formalism.

Fig. 5.1 (a) **Model 1** with three hydrogen bound benzo-15C5 molecules and three perchlorate counter anions; (b) **Model 2** including only the coordinating water molecules.

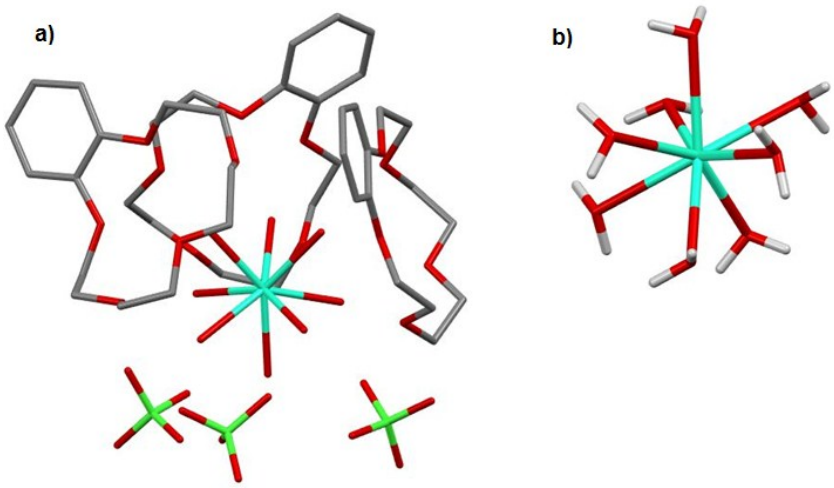

Table 5.1 (left) long basis sets and(right) short basis sets used for each structural model.

Long Basis Sets	
Dy	ANO-RCC-VQZP
O_{coord}	ANO-RCC-VTZP
O	ANO-RCC-VDZP
Cl	ANO-RCC-VDZP
C	ANO-RCC-VDZP
H	ANO-RCC-VDZP

Short Basis Sets	
Dy	ANO-RCC-VDZP
O	ANO-RCC-VDZ
H	ANO-RCC-VDZ

Table 5.2 Energies of the eight Kramers doublets (KD) in the $^6H_{15/2}$ multiplet

KD	Model 1 short (cm^{-1})	Model 1 Long (cm^{-1})	Model 2 Short (cm^{-1})	Model 2 long (cm^{-1})
1	0.00	0.00	0.00	0.00
2	25.55	12.92	17.53	24.86
3	72.07	43.54	45.47	37.45
4	92.18	65.69	78.57	64.80
5	137.97	114.95	123.39	109.42
6	157.57	127.57	139.81	124.99
7	184.63	146.25	163.99	153.90
8	569.53	520.81	519.62	493.81

Table 5.3: g-tensors of the eight Kramers doublets (KD) of the $^6H_{15/2}$ multiplet.

KD		Model 1 Short	Model 1 Long	Model 2 Short	Model 2 Long
1	g_x	0.15230	0.34925	0.25181	0.17539
	g_y	0.23688	1.04049	0.54358	0.60276
	g_z	19.47789	18.40045	19.30460	18.70444

2	g_x	0.27928	0.05088	0.20732	0.51926
	g_y	0.47063	0.51400	1.07942	0.92606
	g_z	17.37565	17.43218	16.47758	17.93311
3	g_x	1.81422	1.91173	2.67007	2.96932
	g_y	3.90371	3.26142	4.25130	4.45079
	g_z	12.97951	13.54675	13.50178	13.69288
4	g_x	1.72513	9.38593	8.71331	0.94389
	g_y	4.95520	6.28668	7.12959	5.49821
	g_z	9.25547	2.66812	0.16044	10.26467
5	g_x	2.01703	1.62801	0.80271	1.77971
	g_y	3.59845	2.49449	4.91717	2.81536
	g_z	12.98379	8.57434	10.985669	12.70925
6	g_x	0.50607	9.93759	9.19074	0.83293
	g_y	1.49166	6.33552	5.93763	0.93475
	g_z	17.90282	1.43966	0.81720	11.16628
7	g_x	1.32591	2.13506	1.14921	1.06758
	g_y	1.92365	6.45724	4.53106	2.65314
	g_z	15.81185	11.51571	15.51931	17.53194
8	g_x	0.00077	0.00110	0.00000	0.00171
	g_y	0.00173	0.00214	0.00000	0.00297
	g_z	19.86937	19.95836	19.86328	19.85986

Table 5.4 Difference between the main magnetic axes of the eight Kramers doublets in the $^6H_{15/2}$ multiplet.

KD	Model 1 short (°)	Model 1 Long (°)	Model 2 Short (°)	Model 2 long (°)
1	0.00	0.00	0	0.00
2	20.49	19.31	15.54	34.51
3	117.63	119.57	78.96	90.55
4	41.36	56.60	44.49	59.73
5	37.58	49.52	17.35	41.36
6	22.19	55.67	103.09	48.09
7	114.26	118.19	113.71	77.99
8	8.46	13.22	102.7	96.14

Fig. 5.2 Main magnetic axes and relaxation pathways for Model 1 (short basis set)

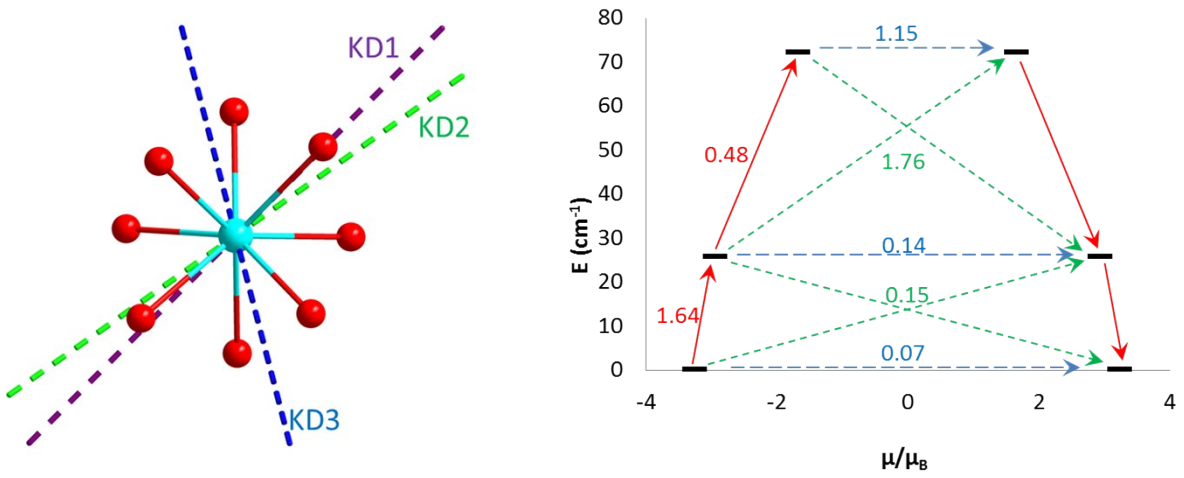

Fig. 5.3 Main magnetic axes and relaxation pathways for Model 1 (long basis set)

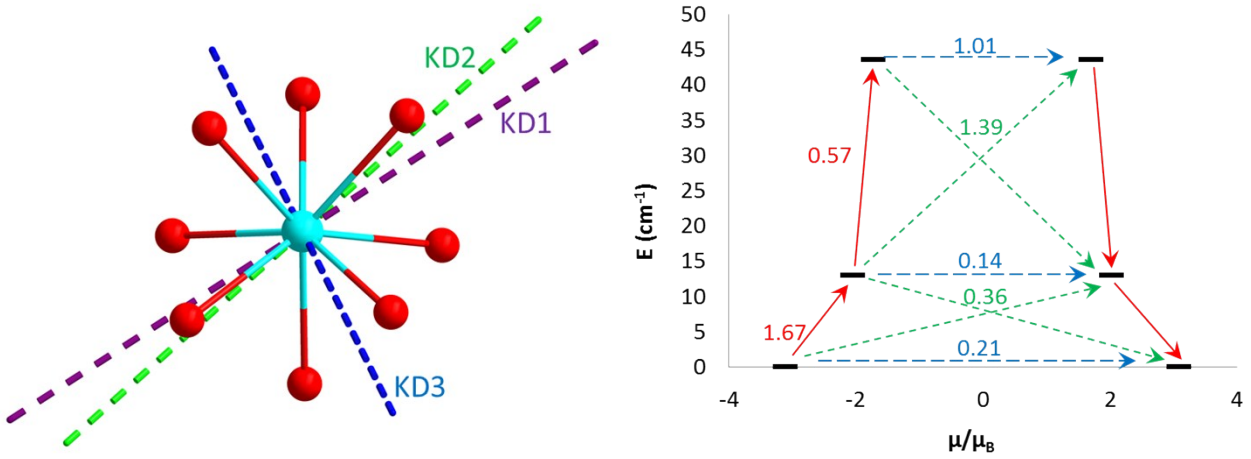

Fig. 5.4 Main magnetic axes and relaxation pathways for Model 2 (short basis set)

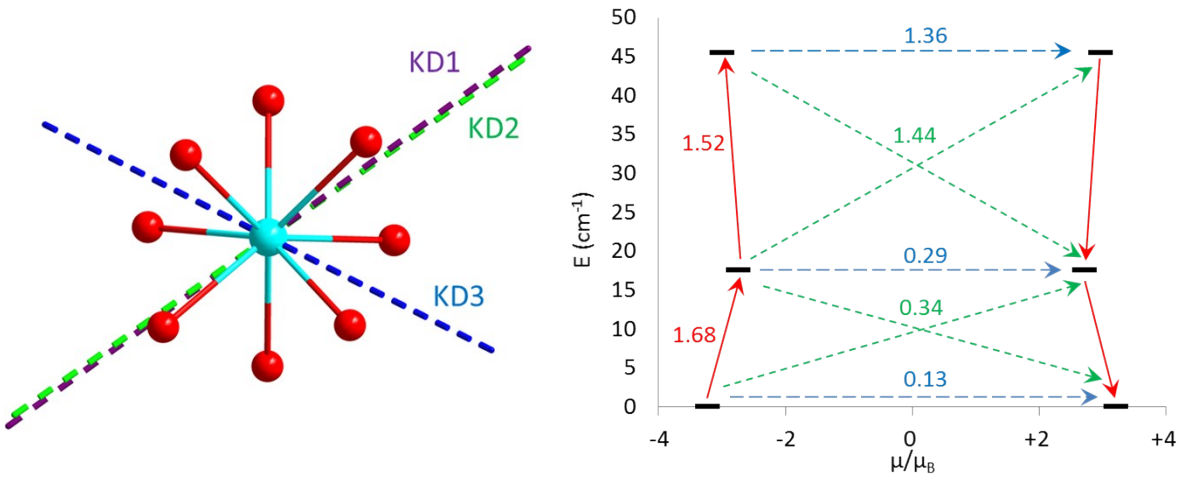

Fig. 5.5 Main magnetic axes and relaxation pathways for Model 2 (long basis set)

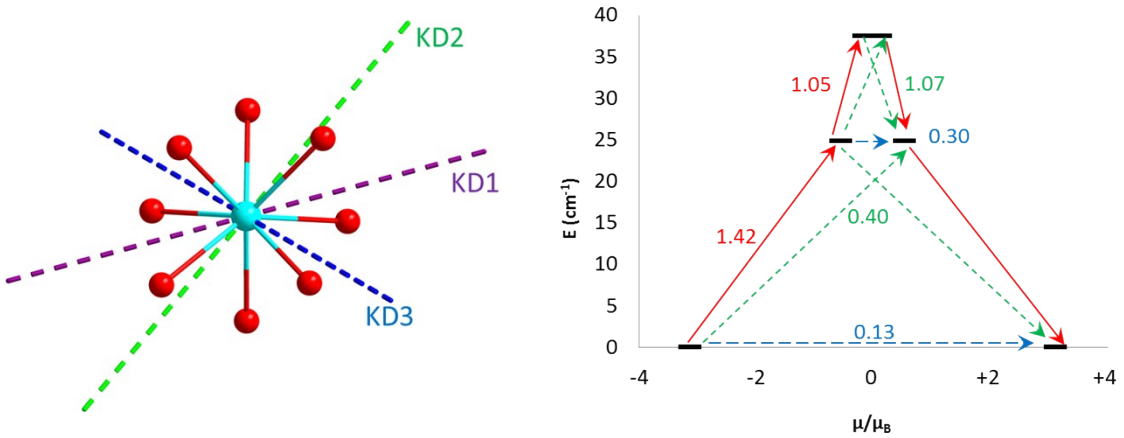

Table 5.5 Computed crystal field parameters for the four models of the complex using the CASSCF/RASSI wavefunctions.

The crystal field Hamiltonian:

$$H_{CF} = \sum_{k,q} B_q^k O_q^k$$

B_q^k is the crystal field parameter and O_q^k is the extended Stevens operator. The quantization axis was chosen as the main magnetic axis of the ground Kramers Doublet.

k	*q*	B_q^k Model 1 Short	B_q^k Model 1 Long	B_q^k Model 2 Short	B_q^k Model 2 Long
2	-2	2.3877136	2.5264830	2.3173897	2.5234365
	-1	0.5573864	-0.5581149	0.3509611	-0.6506982
	0	-1.6866326	-1.4416573	-1.5404061	-1.4488759
	1	0.0791404	-0.3372874	-0.4425036	-0.3536646
	2	1.4970987	-0.1195828	-0.3083320	-0.2936741
4	-4	0.0421639	0.0042569	0.0042211	-0.0015332
	-3	-0.0098588	-0.0298887	-0.0104997	-0.0300936
	-2	-0.0186180	-0.0183344	-0.0206006	-0.0182073
	-1	0.0007881	0.0055049	-0.0011925	0.0065336
	0	0.0016525	0.0017039	0.0018043	0.0017416
	1	0.0041007	0.0109261	0.0069731	0.0114432
	2	-0.0082744	0.0052295	0.0040592	0.0066066
	3	-0.0085059	0.0116407	-0.0107233	0.0160401
	4	-0.0056692	-0.0427308	-0.0408991	-0.0435595
6	-6	0.0001560	-0.0002909	-0.0003262	-0.0003116
	-5	-0.0001786	0.0001596	0.0000586	0.0002205
	-4	-0.0001527	0.0000219	0.0000296	0.0000413
	-3	0.0000233	0.0001072	0.0000314	0.0000973
	-2	0.0001739	0.0001780	0.0002290	0.0001822
	-1	-0.0001119	-0.0000344	-0.0000405	-0.0000441

0	-0.0000003	0.0000022	0.0000009	0.0000021
1	-0.0000557	-0.0001688	-0.0000719	-0.0001840
2	0.0001306	-0.0000005	0.0000137	-0.0000138
3	0.0000540	-0.0001879	-0.0000755	-0.0002217
4	0.0000748	0.0001449	0.0001852	0.0001471
5	0.0001246	0.0002325	-0.0000131	0.0002207
6	-0.0002692	-0.0000605	-0.0000499	-0.0000006

5.2 Discussion

All four models reveal the wavefunctions of the ground state KD 1± are comprised of a large contribution from the $m_J = \pm 15/2$ states and the first excited state KD 2± includes a large contribution from the $m_J = \pm 13/2$. This however dramatically changes for the second excited state which includes nearly an equal contribution of all positive or negative m_J states for the respective wavefunction in the doublet. This likely contributes to the dramatic change in the projection of the main magnetic axis of the second excited state Kramers doublet relative to KD(1±) and KD(2±), supporting our argument that spin-lattice relaxation becomes dominant. The calculated g-tensors for KD(1±) to KD(3±) reveal that there is a small but significant transverse component in the ground and first excited state, consistent with the observation of quantum tunnelling, but that this transverse component is much more pronounced in the second excited state Kramers doublet. It should also be noted that these calculations are in agreement with previous calculations on a model $[Dy(OH_2)_8]^{3+}$ complex which also shows that the ground state KD possesses significant transverse anisotropy.[7]

Interestingly, the basis set size plays a very minor role in determining whether relaxation via the second excited state is present or not. For this complex, the presence of relaxation mechanisms via the second excited state are greatly influenced by the ligand field where the crown ether ligands and PF_6 counterions promote spin lattice relaxation as in Model 1, or the absence of the counterions leads to a greater contribution from a thermal relaxation pathway as in Model 2. In this respect, for Model 1, the calculations are consistent with a higher U_{eff} relaxation pathway involving the second excited state that is reduced by Orbach relaxation, supporting our ac magnetic susceptibility studies. This is evident in the magnitudes of the matrix elements between the spin-states, since the average matrix elements between the KD2 (-) and the KD3 (+) states are very large, whereas the elements between the KD2(-) and the KD2(+) states are substantially smaller. Since these elements correspond to transition moments between the two states, it strongly suggests that Orbach processes are operational. In addition, the angle between the main magnetic axes of the KD2 and KD3 states in Model 1(long basis set) is 120°, consistent with previous reports that perpendicular angles facilitate Orbach relaxation mechanisms.[8]

As previously mentioned, the direction of the anisotropy axes are strongly influenced by the ligand field in all four models. Both the coordinated water molecules and the PF_6 counterions play an important role in the orientation of the easy axes. For all models, the axial components of the crystal field parameters (B, q = 0) change sign between the 2nd rank (k = 2) and the 4th rank (k = 4) which supports a change in the energy level pattern and therefore may affect the orientation of the magnetic axes.[9] The

easy axes are based on the main magnetic axis using the pseudo-spin formalism S = ½ and are centered on a mirror plane parallel to the pseudo four-fold rotation axis. A similar outcome was reported by Sessoli *et al.* for Na{Dy(DOTA)(H_2O)}]·4H_2O,[10] where the orientation of the protons of a coordinated water molecule strongly influence the direction of the vector of the main magnetic axis which is also not linked to the idealized four-fold symmetry axis of the complex. In complex (**4**), the orientations of the protons of the eight coordinated water molecules are also involved in H-bonding interactions to the three uncoordinated crown ether ligands and/or the PF_6 counterions within the crystal lattice and most appear to strongly influence the orientation of the magnetic anisotropy in all four models studied.

Based on this detailed analysis we conclude that Model 1 (long basis set) provides the most accurate description of our complex since in addition to eight coordinated water ligands, it also takes into account the H-bonded PF_6 counter ions in the crystal structure. The energy separation between the ground and first excited state KDs determined for this model (13 cm^{-1}) is in good agreement with the effective energy barrier of 10 cm^{-1} determined from the ac susceptibility studies, where the smaller value of the U_{eff} is consistent with QTM which were supressed in the ac susceptibility studies via application of a small dc field.

S-6 Photoluminescence data

6.1 Experimental

Luminescence data were recorded at 300 and at 12 K using a modular double grating excitation spectrofluorimeter with a TRIAX 320 emission monochromator (Fluorolog-3, Horiba Scientific) coupled to a R928 Hamamatsu photomultiplier, using a front face acquisition mode. The excitation source was a 450 W Xe arc lamp. The emission spectra were corrected for detection and optical spectral response of the spectrofluorimeter and the excitation spectra were corrected for the spectral distribution of the lamp intensity using a photodiode reference detector. The room temperature time-resolved emission spectra and emission decay curves (10^{-6}-10^{-9} s) were recorded on a Fluorolog TCSPC spectrofluorimeter (Horiba Scientific) coupled to a TBX-04 photomultiplier tube module (950 V), 200 ns time-to-amplitude converter and 70 ns delay. The excitation source was a Horiba-Jobin-Yvon pulsed diode (NanoLED-390, peak at 390 nm, 1.2 ns pulse duration, 1 MHz repetition rate and 150 ns synchronization delay). The emission decay curves (10^{-6}-10^{-2} s) were recorded at room temperature with a Fluorolog TCSPC spectrofluorometer (Horiba Scientific) coupled to a TBX-04 photomultiplier tube module (950 V), 50 µs delay. The exciting source was a Horiba Scientific pulsed diode light source (SpectraLED-355, peak at 356 nm).

Fig. 6.2 (a) Emission and (b) excitation spectra for (4) acquired at 300 K (blue lines) and at 14 K (black lines) for (**4**) excited at 365 nm and monitored at 574 nm respectively. In the excitation spectra the ground state ($^6H_{15/2}$) is omitted for simplicity and only the excited states are assigned.

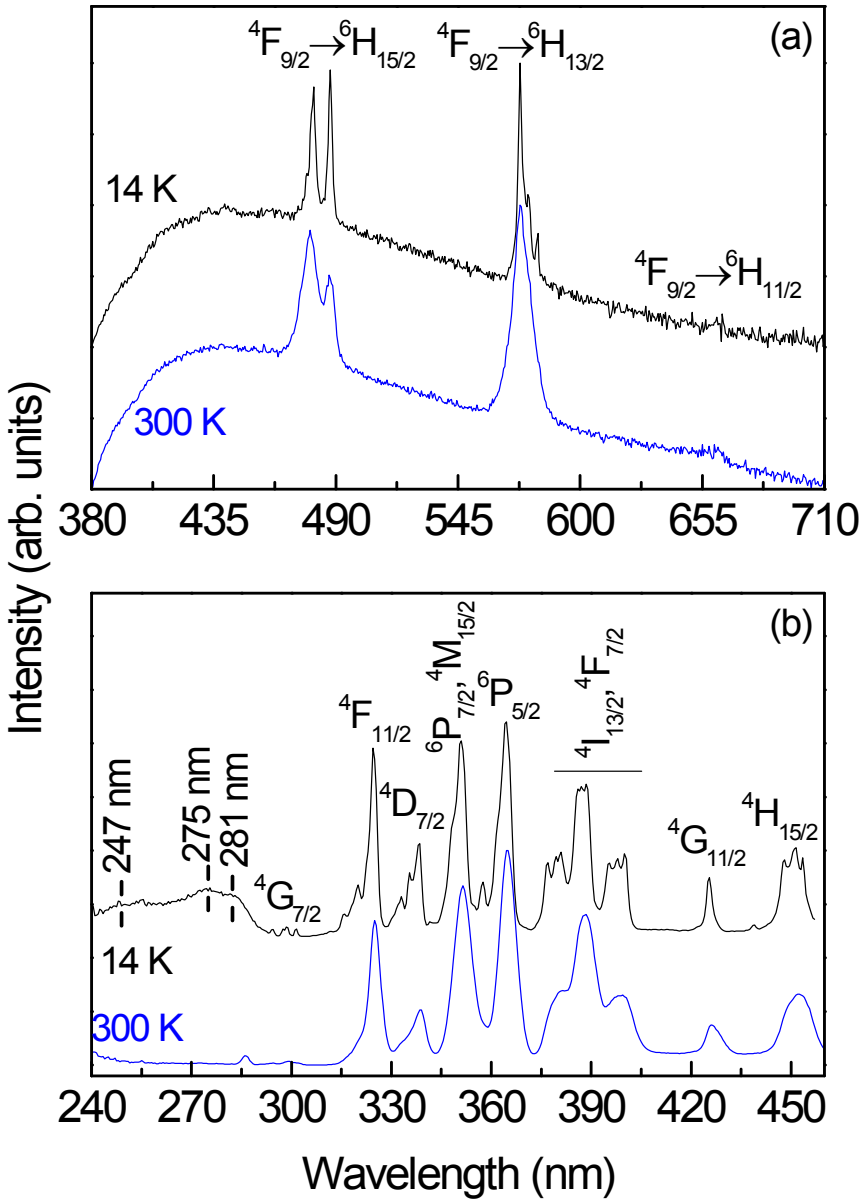

Fig. 6.3 Excitation spectrum acquired at 14 K for (**4**) monitored at 440 nm.

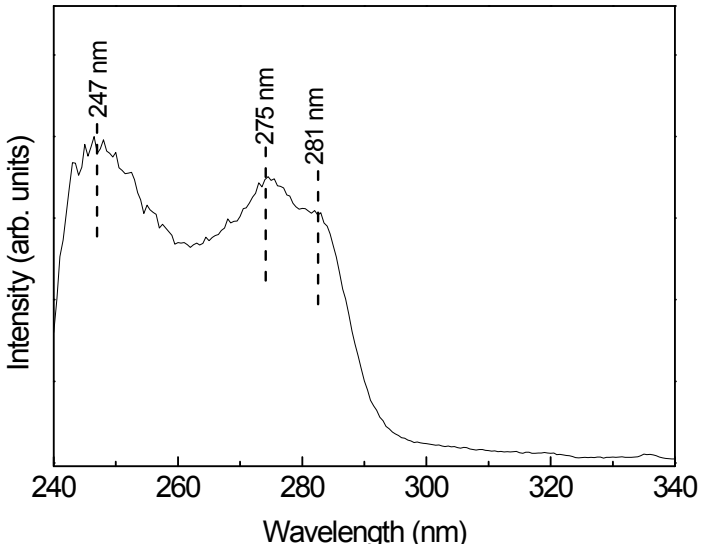

Fig. 6.3 Emission decay curve (300 K) for (4) monitored at 577 nm and excited at 390 nm. The solid lines represent the single exponential fit. The inset shows the fit regular residual plot.

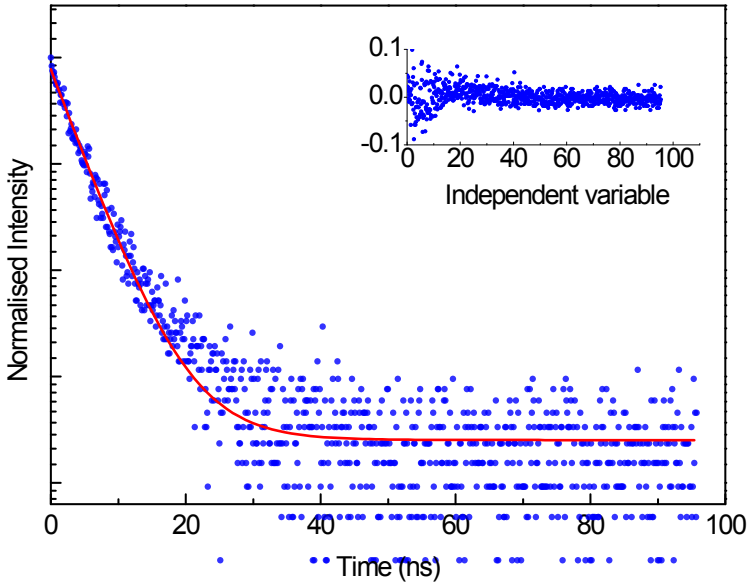

Table 6.1 Energy peak position (E, ± 3.0 cm^{-1}) and full-width-at-half maximum (fwhm, ± 5.0 cm^{-1}) of the $^4F_{9/2}\rightarrow{}^6H_{15/2}$ Stark components (identified from 1-10) determined from the experimental emission spectrum (acquired at 12 K and excited at 365 nm) best fit using a 10-component Gaussian fit.

Assignment*	*E*	*fwhm*
10	20390.0	58.8
9	20474.0	69.6
8	20540.0	70.6
7	20615.0	70.6
6	20696.0	82.4
5	20786.1	72.4
4	20844.0	76.5
3	20921.0	76.5
2	20938.0	70.6
1	21000.0	61.0

*The assignment is illustrated in Figure 5 in the manuscript.

6.2 Discussion

The emission and excitation spectra for **4** acquired at 300 and 14 K reveal a broad band comprising three components at *ca.* 247, 275 and 281 nm associated with ligand emission, Fig. 6.3. In addition, a series of sharp lines arising from Dy(III) transitions occurring between the electronic levels of the $4f^5$ configuration, namely the $^6H_{15/2}$ ground level and the $^4G_{7/2}$, $^4F_{11/2}$, $^4D_{7/2,5/2}$ and $^3H_{7/2}$ excited states are also observed. Apart from a decrease in the full-width-at-half-maximum of the intra-$^4f_5$ transitions, the emission is almost independent of the temperature. We also note that the intra-$^4f_5$ components display lower relative intensity, so that we may readily infer that the Dy(III) excited states are mainly populated via an efficient ligand-sensitization mechanism. The room-temperature $^4F_{9/2}$ emission decay curve was monitored around the more intense transition of the Dy(III) ion ($^4F_{9/2}\rightarrow{}^6H_{13/2}$, 577 nm). The curve is well described by a single exponential function (Fig. 6.3), yielding a lifetime value of $(5.75 \pm 0.05) \times 10^{-9}$ s.

The following methodology was used in order to determine the energy barrier, ΔE, based on the emission spectrum. Examining the spectrum, it is possible to discern, at least, 9 components (marked with green arrows in Figure 6.1). Taking into consideration that the Dy(III) ions have a local D_{4d} symmetry we may expect the splitting of the electronic levels ($^4F_{9/2}$ and $^6H_{15/2}$) into the maximum number of allowed components, namely $(2J + 1)/2$, which means that 5 and 8 components are expected for $^4F_{9/2}$ and $^6H_{15/2}$, respectively. Thus, at least, 8 Stark components are expected for the $^4F_{9/2}\rightarrow{}^6H_{15/2}$ transition if only the lower-energy Stark component of the $^4F_{9/2}$excited state is populated and all the transitions end at the lower-energy Stark of the ground multiplet $^6H_{15/2}$. Since 9 components are clearly present (green arrows, Figure 4a), it readily points out that the second Stark component of the $^4F_{9/2}$ excited state must also be populated. This is a feasible situation, since the energy difference between that first Stark component and the

second one is typically of the order of 60 cm^{-1}, as reported in the literature for several compounds.[10] Thus, at 15±3 K, it may be populated (up to 2 %, considering a classical Boltzmann distribution). This rational, was behind the proposed 10-fit components. Moreover, considering transitions ending at excited Stark components of the $^6H_{15/2}$ multiplet, the energy of the Stark components of this multiplet does not match with what was reported. To locate the first and second Stark components of the $^4F_{9/2}$ level, the low-wavelength region of the spectrum was inspected, so that the later component was tentatively set at 60 ±10 cm^{-1} above the clearly express transition ascribed to the 0→0 transition. Then, the 9 remaining components were fitted using a Gaussian function, whose energy was constrained to the peak position analysis based on the spectrum observation (green arrows, Figure 6.1) taking into account the experimental uncertainty (±3 cm^{-1}); the full-width-at.-half-maximum and the relative intensity was free to vary. The energy peak position and full-width-at-half maximum resulting from the fit are summarized in Table 6.1.

Fig. 6.1 Magnification of the $^4F_{9/2}\rightarrow{}^6H_{15/2}$ transition at 12 K and excited at 365 nm. Multi-Gaussian functions envelope fit (circles) and the components arising from the (orange shadow) first and (purple shadow) second $^4F_{9/2}$ Stark sublevels to the $^6H_{15/2}$ multiplet.

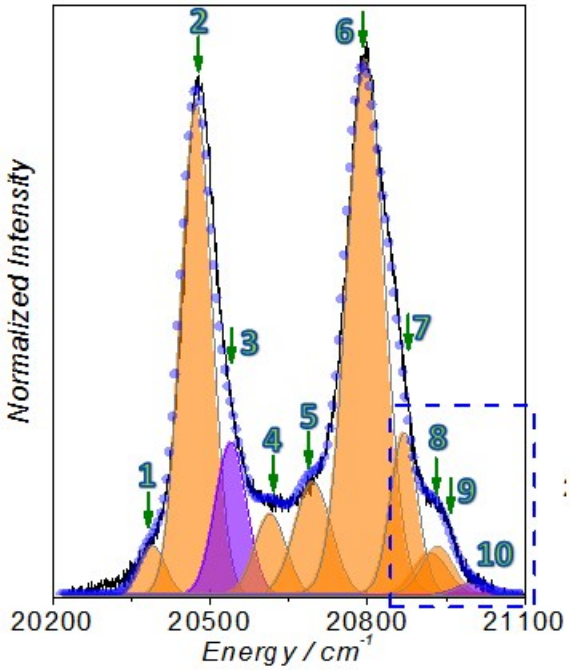

S-7 References

[1] Bruker, Bruker AXS Inc. Madison, Wisconsin, USA, 2007.

[2] G. M. Sheldrick, University of Göttingen, Germany, 1996.

[3] G. M. Sheldrick, Acta Cryst. A, 2007, 64, 112.

[4] H. Zabrodsky, S. Peleg and D. Avnir, D. *J. Am. Chem. Soc*., 1992, **114**, 7843.

[5] Y. -N. Guo, G.-F. Xu, Y. Guo and J. Tang, *Dalton Trans*., 2011, **40**, 9953.

[6] (a) F. Aquilante, L. De Vico, N. Ferré, G. Ghigo, P.-A, Malmqvist, P. Neogrády, T. B, Pedersen, M. Pitoňák, M. Reiher, B. O. Roos, L. Serrano-Andrés, M. Urban, V. Veryazov and R. Lindh, *J. Comp. Chem*. 2010, **31**, 224; (b) V. Veryazov, P.-O. Widmark, L. Serrano-Andrés, R. Lindh and B. O. Roos, *Int. J. Quant. Chem.,* 2004, **100**, 626; (c) G. Karlström, R. L. Lindh, P.-A. Malmqvist, B.O. Roos, U. Ryde, V. Veryazov, P.O. Widmark, M. Cossi, B. Schimmelpfennig, P. Neogrady and L. Seijo, *Comp. Mater. Sci.,* 2003, **28**, 222.

[7] S.L. Langley, L. Ungar, N.F. Chilton, B. Moubaraki, L.F. Chibotaru and K.S. Murray, *Inorg. Chem*., 2014, **53**, 10835.

[8] E. Lucanni, M. Briganti, M. Perfetti, L. Vendier, J.-P. Costes, F. Totti, R. Sessoli, L. Sorace, *Chem. Eur. J*. 2016, 22, 5552.

[9] S. K. Singh, T. Gupta, M. Shanmugam and G. Rajaraman, *Chem.Commun.,* 2014, **50**, 15513.

[10] G. Cucinotta, M. Perfetti, J. Luzon, M. Etienne, P.-E. Car, A. Caneschi, G. Calvez, K. Bernot and R. Sessoli, Angew. Chem. Int. Ed., 2012, **51**, 1606.